GEOLOGY

Pulsed volcanic sulfur emissions linked to the end-Triassic terrestrial crisis

Linhao Fang[1,2]*, Robert J. Newton[3]*, Xiaoyu Zhang[4], Hongjia Li[4], Guangli Wang[1,2]*, Shenghui Deng[5], Paul B. Wignall[3]*, Yuanzheng Lu[5], Chaokun Zhang[4], Meijun Li[1,2], Huaichun Wu[6], Tianchen He[7], Benzhong Xian[1,2], Shengbao Shi[1,2], Lei Zhu[1,2], Simon H. Bottrell[3], Stephen P. Hesselbo[8]

The end-Triassic mass extinction (ETE) was triggered by Central Atlantic Magmatic Province (CAMP) volcanism, which released voluminous carbon dioxide, sulfur dioxide, and halogens into the atmosphere, affecting marine and terrestrial ecosystems, but the mechanism driving terrestrial crisis remains unclear. Here, we investigate two terrestrial Triassic-Jurassic sections in high- and low/middle- paleolatitudes, finding synchronous anomalies of mercury concentration, sulfur (S) isotopes, S-associated molecular fossils, and biomarkers (retene, pimanthrene, and coronene), indicating that peak volcanic sulfur deposition coincided with floral diversity loss and fern spikes, and intensified high-temperature wildfires over an interval of ~60,000 years. We propose that the pulse of maximum CAMP eruptions rapidly increased volcanic-S influxes (acid rain) to terrestrial basins, leading to catastrophic plant dieback during the ETE. The consequent creation of moisture-free biomass supplied fuel for increasingly frequent and widespread intense wildfires, occurring even on a global scale.

INTRODUCTION

The end-Triassic mass extinction (ETE) at 201.6 million years ago (Ma) (*1*, *2*) was one of the most severe biotic crises of the Phanerozoic, representing one of the "Big Five" in Earth history (*3*, *4*). The coeval Central Atlantic Magmatic Province (CAMP) volcanism emplaced a large volume of flood basalt flows [2 to 4 × 10^6 km^3; (*5*)] through a series of geologically short eruptive episodes (possibly four major pulses) over ~600 ± 20 thousand years (kyr) (*2*, *6*). Volatile emissions of SO_2 were up to 16,000 to 32,000 gigatonnes (*7*) and CO_2 up to 100,000 gigatonnes (*8*), together with other volatiles (*9*). Sills likely baked carbon-rich sediments and evaporites in the upper crust of the Amazonas and Solimões basins, injecting additional quantities of CO_2 and SO_2 into the atmosphere (*10*). The environmental effects of these combined emissions are invoked to have caused the marine extinctions (*4*) and terrestrial crisis (*11*–*22*) that coincided with fern spikes (*11*, *15*, *16*, *18*, *19*, *21*, *23*) during the ETE. Long-term warming due to the emission of greenhouse gases is likely to have persisted into the Early Jurassic (*13*, *14*, *24*).

Although terrestrial ecosystem turnover (both floral and faunal) is widely reported for the ETE [e.g., *11*–*22*, *25*–*27*], the mechanism remains controversial. The geologically rapid, two-phased loss of floral biodiversity (*11*–*14*, *18*–*22*) and widespread rise in intense wildfires (*11*, *19*–*21*, *28*) are recorded from the ETE interval. Regionally variable climatic changes, due to global warming, have been proposed as a contributing cause of the vegetation turnover (*29*, *30*). An increase in storminess and frequency of lightning as well as the shift to more flammable plant types could have ignited more forest fires (*31*). However, global CO_2 greenhouse effects last for long periods of time [>100 kyr; (*29*, *30*, *32*)] and are difficult to link with the shorter-lived (<100 kyr) turnovers in terrestrial ecosystems, such as the fern spike (*11*, *15*, *19*, *21*, *23*, *33*), rapid pulses of increasingly intense wildfires [marked by coronene index and/or coronene abundance spikes; (*21*, *28*, *34*–*36*), and charcoal; (*20*, *31*, *37*)], and deforestation associated with catastrophic soil loss (*38*).

The emission of voluminous SO_2 is commonly thought to do less long-term damage to ecosystems than CO_2, due to its geologically short residence time in the atmosphere (*39*, *40*). However, SO_2 aerosols can decrease global temperatures, potentially deplete ozone over years to decades (*41*, *42*), and lower the pH in soils (*43*). The total mass of sulfur released from CAMP volcanism was 16,000 to 32,000 gigatonnes of SO_2 (0.8 to 1.6 × 10^{19}g S) (*7*) and only represents a small fraction of the seawater reservoir, even accounting for its much smaller size of oceanic sulfur reservoir at this time (*44*), and is thus unlikely to be detectable in marine records (*45*). By contrast, this released mass represents an anomalously high flux of S into sedimentary systems on land, which are typically low in S and have varying buffering capacities. Thus, the terrestrial sedimentary systems are likely to be more sensitive to, and more able to record, sulfuric acid rain than marine settings (*46*, *47*). However, direct evidence for such acid rain has not been found because robust proxies are challenging to preserve in terrestrial sediments. The causal links between SO_2 precipitation (and that of associated halogens) and terrestrial floral turnovers have therefore been difficult to verify.

In this study, we report S isotope and organic geochemical evidence for acid rain synchronous to the CAMP volcanism from two well-exposed terrestrial sections across the Triassic-Jurassic boundary (TJB). Both are located in western China: the high-paleolatitude (~60°N) Haojiagou (HJG) section in the Junggar Basin and the lower paleolatitude (~30° to 40°N) Qilixia (QLX) section in the Sichuan Basin (Fig. 1 and fig. S1). Here, we present records of mercury (Hg) concentration, biomarkers for wildfire, S deposition and higher plants, and isotopic data from total S in terrestrial sediments to test the hypothesis of

[1]State Key Laboratory of Petroleum Resources and Engineering, China University of Petroleum (Beijing), Beijing 102249, China. [2]College of Geosciences, China University of Petroleum (Beijing), Beijing 102249, China. [3]School of Earth and Environment, University of Leeds, Leeds LS2 9JT, UK. [4]School of Earth and Space Sciences, Peking University, Beijing 100871, China. [5]Research Institute of Petroleum Exploration and Development, PetroChina, Beijing 100083, China. [6]School of Ocean Sciences, China University of Geosciences, Beijing 100083, China. [7]College of Oceanography, Hohai University, Nanjing 210024, China. [8]Camborne School of Mines, Department of Earth and Environmental Sciences, University of Exeter, Penryn TR10 9FE, UK.
*Corresponding author. Email: linhao.fang@cup.edu.cn (L.F.); r.j.newton@leeds.ac.uk (R.J.N.); sydxwgl@cup.edu.cn (G.W.); p.b.wignall@leeds.ac.uk (P.B.W.)

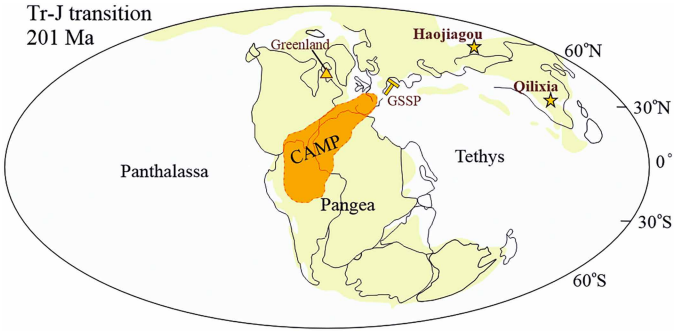

Fig. 1. Global paleogeographical map of the Triassic-Jurassic (Tr-J) transition (~201 Ma), showing the sampling locations and two other key reference sections. Stars represent the HJG section at ~60°N, high paleolatitude and QLX section at ~30° to 40°N (low/middle paleolatitude) in the Junggar Basin and Sichuan Basin of China, respectively. Triangle marks the terrestrial Astartekløft section, East Greenland. Hammer represents the marine GSSP for the TJB at Kuhjoch, Austria. The paleogeographical location and the extent of CAMP are based on (*5*). Paleogeographic map is modified from (*44*) (CC BY 4.0, https://creativecommons.org/licenses/by/4.0/deed.en).

whether terrestrial ecosystem turnover was primarily driven by pulsed S releases from the maximum of CAMP volcanism during the ETE.

Geological setting and age framework

The HJG and QLX sections are well exposed with continuous outcrop through the ETE onset and the TJB (figs. S1 and S2). The HJG section consists of the Haojiagou and Badaowan formations, where the succession is dominated by alluvial and swamp facies (*48*). The QLX section consists of the Xujiahe and Zhenzhuchong formations of similar sedimentary facies (*22*). The base of the Badaowan Formation (bed 45 to bed 48; Fig. 2) has a low plant biodiversity according to palynological records, and beds 45 to 48 coincide with the peak fern spike in the HJG section (*19*, *23*). Previous paleontological and palynological studies show a low-diversity horizon (palynological assemblage 4-PA 4; Fig. 2), coinciding with the highest fern spike at the base of the Zhenzhuchong Formation in the QLX section (*22*).

The HJG section has been well studied. The biostratigraphy (including plant macrofossils and palynology), carbon isotope excursions (CIEs), and astrochronology indicate that ETE and TJB lie around beds 43 to 48 (Figs. 2 and 3) (*23*, *48*–*51*). In the QLX section, the age framework is based on palynostratigraphy (*22*), chemostratigraphy (i.e., CIE and Hg spikes) (*51*), and astrochronology integrated with magnetostratigraphy (*52*); and thus, the ETE and TJB are placed around beds 18 to 19 (Figs. 2 and 3). As a result, the ETE horizon and TJB at HJG and QLX can be correlated with the marine sections at the global stratotype at Kuhjoch, Austria (Fig. 3) and the well-known St. Audrie's Bay section, England. The timing of CAMP volcanism relative to the ETE and TJB hinges on integrated biostratigraphic, chemostratigraphic, and magnetostratigraphic studies (*22*, *23*, *48*–*52*), which allow a robust, comparable chronostratigraphic framework with floating astrochronological scales for sections at HJG (405 kyr long eccentricity) and QLX (~100 kyr short eccentricity) (Fig. 2 and figs. S2, S3, and S5).

RESULTS

Volcanic input: Hg/TOC and Hg

The ratio of mercury to total organic carbon (Hg/TOC) and Hg concentration are plotted (Figs. 2 and 3). Hg is primarily hosted in the organic matter, when the total sulfur is less than 1% (*53*), which is the case for this study. The concentrations are normalized for samples with TOC content >0.2 and <0.2%, respectively, and plotted in different symbols and superimposed (fig. S2), following published methods (*51*, *54*). The curves of Hg/TOC in both sections show similar stratigraphic patterns (Fig. 2).

In the HJG section, the Hg/TOC ratio shows relatively high values between ~55 and ~130 m (Fig. 2), corresponding to an ~700-kyr interval, based on the astronomical floating timescale (*50*). About six discrete Hg/TOC peaks are presented in this interval. The highest Hg/TOC peaks are in the upper half of the ETE interval and occurred over ~60 kyr. Smaller peaks of Hg/TOC are present above and below the level of the ETE. In the QLX section, Hg/TOC values are relatively high between ~100 and ~140 m in height (Fig. 2), corresponding to a period of ~700 kyr based on astronomical floating scales (*52*). Three or four discrete Hg/TOC peaks are present. The highest Hg/TOC values occur in the lower half of the ETE interval with smaller Hg/TOC peaks below and above.

The Hg/TOC curves in the HJG and QLX sections are broadly similar (Fig. 3). When these two sections are correlated to other Triassic-Jurassic (Tr-J) sections worldwide, the highest peak values of Hg/TOC in the ETE interval coincide with a broad positive CIE in each section (Fig. 3). The highest values of Hg/TOC in the terrestrial sections are two to three times higher than seen in the marine stratotype at Kuhjoch, Austria (Fig. 3) (*55*). Below the ETE horizon, secondary elevated Hg/TOC peaks occur in the four sections. Above the TJB, some elevated Hg/TOC values are observed in three sections, except at Astartekløft in East Greenland (Fig. 3).

Sulfur addition: S isotopes, biomarkers, and S/TOC

In the HJG section (Fig. 2), the sulfur isotope curve derived from the extraction of total sulfur displays multiple fluctuations ranging from approximately −2 to +12‰, with an average background value of around 0 to +3‰. A negative excursion, reaching −2‰, is observed in the upper part of the ETE interval at ~96 m. A positive excursion, reaching +12‰, occurs in the lower part of the ETE interval. The negative sulfur isotope excursion is associated with elevated Hg/TOC, biomarker abundance indicative of higher plant, and polycyclic aromatic hydrocarbon (PAH) concentrations. However, two additional negative excursions of −2‰ at ~20 and ~45 m do not correspond to elevated values of these variables. In the QXL section (Fig. 2), the sulfur isotope curve spans a range from −10 to +30‰, while overall, the values are relatively stable throughout the section, with background values of ~0 to +5‰ prior to and post the ETE interval. A negative excursion reaches −10‰ in the Upper Triassic at ~110 m height. Two additional negative excursions of around −9‰ occur in the upper ETE interval and just above the TJB at ~130 m. All three negative sulfur isotope excursions coincide with elevated Hg/TOC, biomarker abundance indicative of higher plant, and PAH concentrations. A positive S-isotope excursion, reaching +28‰, is observed in the lower part of the ETE interval. Data from both basins present similar trends in $\delta^{34}S$ data (Fig. 2) with increased variability within and around the ETE somewhat coupled to increases in Hg/TOC, although the scale of S-isotope change is muted at HJG compared to QXL.

Stratigraphic plots of dibenzothiophene and benzo-naphthalothiophene with their alkylated homologs (DBTs and BNTs, respectively) at HJG and QLX show similar trends (Fig. 2), although the absolute values vary substantially between the two sections. DBTs and BNTs are thermally stable aromatic sulfur compounds whose

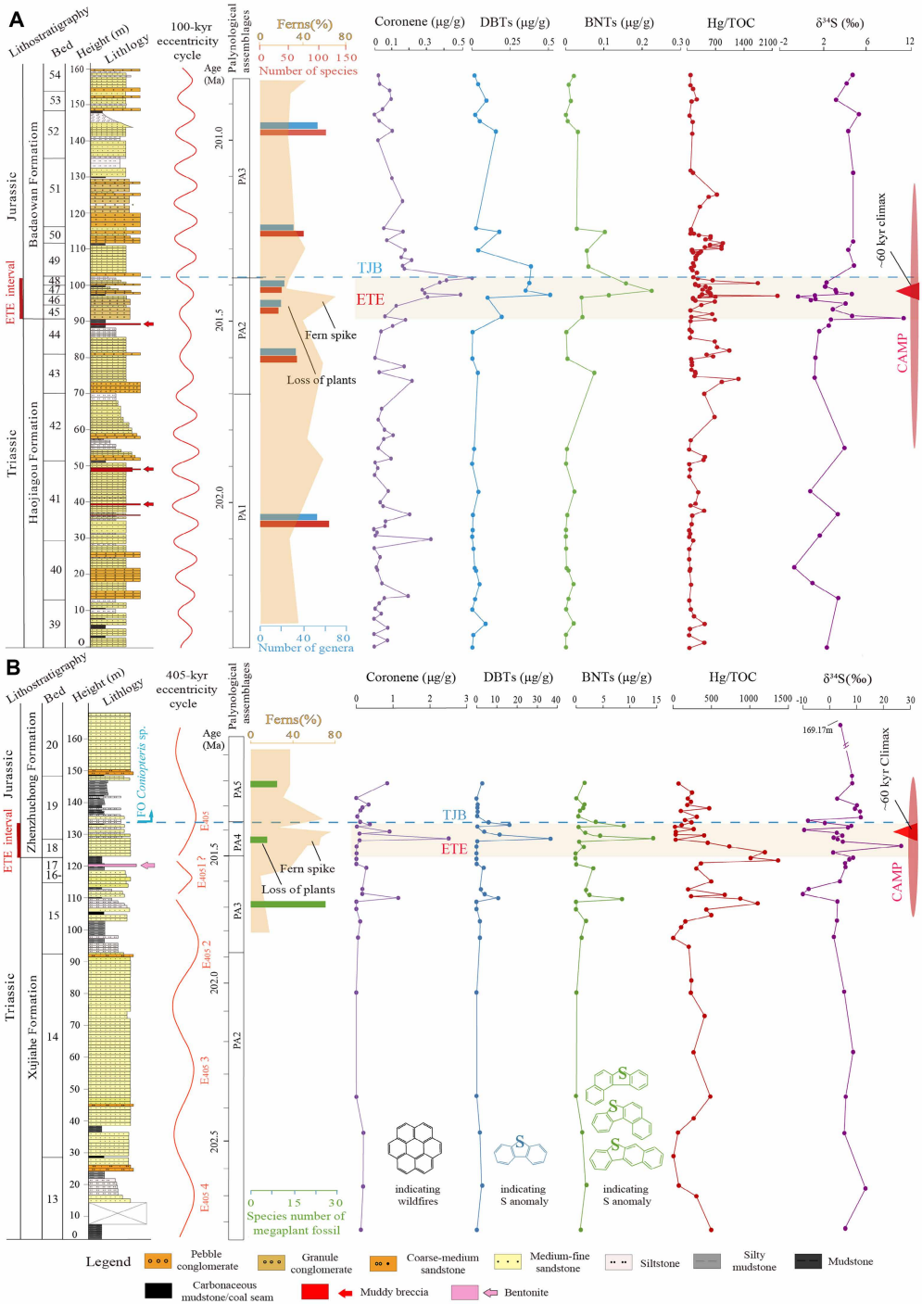

Fig. 2. The Tr-J profiles of the HJG and QLX sections. (**A**) HJG section. (**B**) QLX section. The ETE and TJB are marked by orange shadow and by blue correlative lines. At HJG, the biostratigraphic framework is based on the fossil plants, sporo-pollen and macrospore (*49*), fern spore content (*23*), and carbon isotope stratigraphy (fig. S2) (*23*, *48*, *51*). Onset of the ETE is correlated to the base of bed 45, and marine ammonite-defined TJB is correlated to the base of bed 49 [the stratigraphic correlation line was redrawn based on (*50*)]. At QLX, the biostratigraphic framework is based on the fossil plants, palynology (*22*), and carbon isotope stratigraphy (fig. S2) (*51*). Onset of the ETE horizon and TJB is correlated between the base of bed 18 and the bottom of bed 19, respectively (*51*). The astronomical eccentricity cycles and ages are cited from previous works for HJG (*50*) and QLX (*52*). The orange shadow indicates the ETE interval (lasting ~150 to 200 kyr), and the red triangle on right shadows indicate the CAMP climax (lasting ~60 kyr). The high coronene content is the evidence for intense wildfires. The DBTs and BNTs are sulfur-associated molecular fossils, indicating the extra sulfur influxes interpreted to link with the CAMP-derived sulfuric acid rain. Elevated Hg/TOC is interpreted to record CAMP volcanism. The peaks of coronene, DBTs, and BNTs, and most negative $\delta^{34}S$ excursion are consistently coincident with highest spikes of CAMP climax at HJG and QLX in the two independent terrestrial catchments. In addition, these coincident peaks above agree with the fern spike at HJG and QLX, which suggest a short-lived biological crisis of terrestrial ecosystems in both basins. PA, palynological assemblage; E405, 405-kyr eccentricity cycle.

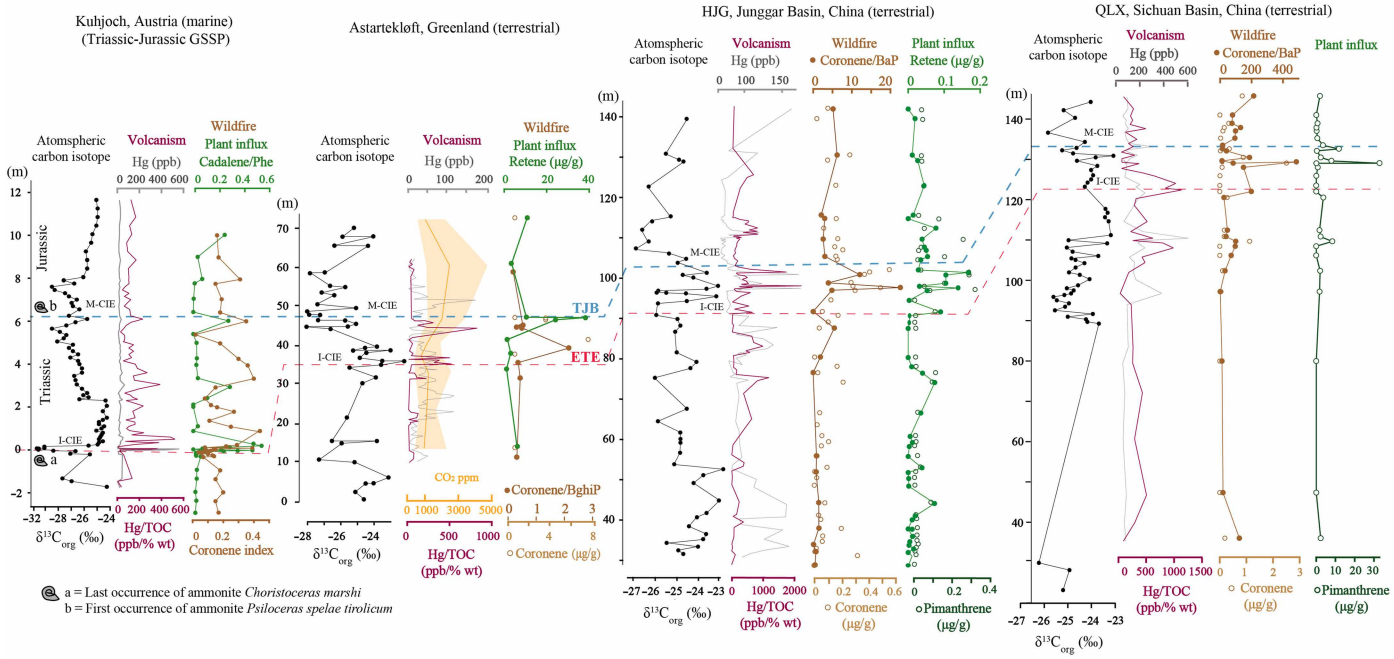

Fig. 3. Stratigraphic correlation of the HJG and QLX sections to key Tr-J sections across the world. Correlation is based on stratigraphic curves of carbon-isotopes and Hg/TOC across the ETE and TJB, constrained by ammonite biostratigraphy and terrestrial palynological records and plant macrofossils (*17*, *33*, *36*). The onset of the ETE (red dotted line) and TJB (blue dotted line) are correlatable between sections. The CO_2 concentration (*30*) and detailed correlation of Hg/TOC is from previous work (*17*, *51*, *55*). The high ratio of coronene relative to BaP or BghiP in the three terrestrial sections and the coronene index in the marine section present as evidence for intense wildfires. Biomarker retene and pimanthrene (and also cadalene/Phe) could reflect the depositional input fluxes of higher plants.

sulfur-rich formation conditions make them indicators of enhanced sulfur input and related environmental change (*56*–*58*). DBTs and BNTs are low in abundance overall in each section, but large peaks (approximately six times the background) are seen in the latest Triassic period and coincide with the ETE horizon (Fig. 2). Above the TJB horizon, one or two other peaks of DBTs and BNTs occur in the HJG section, with no similar peaks at QLX. Below the ETE interval, the secondary peaks of BNTs at HJG and peaks of DBTs and BNTs at QLX occur close to spikes of Hg/TOC (Fig. 2 and fig. S2). The S/TOC trends are broadly comparable between HJG and QLX (fig. S2). The highest S/TOC value occurs above the TJB in each section. Elevated values generally coincide with those of DBTs, BNTs, and Hg/TOC. Outside of a region of elevated S/TOC around the ETE, the S/TOC overall remains low and stable through the profiles at HJG and QLX.

Burial of higher plants: Biomarker proxies

The biomarkers of pimanthrene, retene, and cadalene are primarily derived from the higher plants, and their stratigraphic pattern with normalized abundance indicates a relative change to terrestrial vegetation inputs (*17*, *59*). Pimanthrene trends show similar patterns in the HJG and QLX sections, but the absolute value at QLX is ~70 times greater than at HJG (Fig. 3). The largest peaks of pimanthrene are seen during the ETE, while smaller peaks lie above and below. Otherwise, pimanthrene values are low and stable throughout the two profiles. The retene content resembles that of pimanthrene at HJG and show similarities with the Astartekløft's record from Greenland (Fig. 3). The pimanthrene and retene trends share similarities with the cadalene/Phe seen in the Global Stratotype Section and Point (GSSP) marine section at Kuhjoch, Austria (Fig. 3) (*36*). Overall, pimanthrene, retene, and cadalene/Phe show their highest values in the ETE interval at all localities.

Wildfire records: Coronene

In the HJG section, the coronene content is on average <0.1 μg/g TOC over most of the succession, but shows elevated values (maximum of ~0.6 μg/g TOC) between ~96 and ~103 m height in the upper half of the ETE interval, with the highest value about six times the background average (Fig. 2 and fig. S2) and three smaller peaks in ~36, 73 to 76, and ~130 m (Fig. 2 and fig. S2). In the QLX section, the coronene content is generally low throughout the section with the highest value (~2.6 μg/g TOC) at ~127 m and two secondary peaks at ~110 and ~133 m (Fig. 2). Curves of coronene and coronene/benzo(*a*)pyrene (Bap) show similar patterns in the HJG and QLX sections, and the absolute values of coronene and coronene/Bap at QLX are all consistently higher than those at HJG (Fig. 3). This pattern at HJG and QLX resembles that of coronene/benzo(*g*,*h*,*i*)perylene (BghiP) at Astartekløft, Greenland (*34*) and agrees with coronene index data at Kuhjoch, Austria (Fig. 3) (*36*). The stratigraphic curves of coronene-based proxies from the three terrestrial sections and one marine section all show their maximum values in the ETE interval (Fig. 3). Coronene/Bap values stay low and stable at other levels at HJG and QLX, except for some smaller coronene peaks that coincide with the secondary peaks of pimanthrene and retene (Fig. 3).

Our empirical datasets contribute direct evidence for records of volcanic-S influx in terrestrial catchments and provide previously unrecognized insights into causal and detailed temporal relationships between the CAMP volcanism, CO_2 greenhouse effects, acid

rain, wildfire, and the turnovers of terrestrial ecosystems across the Tr-J transition.

DISCUSSION

Records of CAMP volcanism in two terrestrial basins at the ETE

Peaks in Hg/TOC and Hg concentration can record volcanic activity locally and globally, as Hg is rapidly transported as gas and aerosols via atmospheric circulation (*6*, *55*). Pulses of Hg/TOC are coupled with the positive shifts in the Hg isotope (Δ^{199}Hg) marked with the Hg source of volcanic activities at HJG and QLX around the ETE (fig. S3) (*51*). The Hg/TOC values are considerably higher than baseline between 55 and 130 m height in the section, which corresponds to almost the entire period of CAMP volcanism, lasting for ~700 kyr according to floating astronomical timescales (*50*). The upper ETE interval at HJG is coincident with the highest Hg/TOC (Fig. 2), which is interpreted as the climax of CAMP volcanism, lasting for ~60 kyr. Peak Hg/TOC values are also observed in the late-phase of the ETE in Greenland (Fig. 3) and in marine locations (*6*). At QXL, primary pulses of the CAMP volcanism are identified stratigraphically from 100 to 140 m, based on the interval of relatively high Hg/TOC values. However, the highest peak is at ~123 m, where it seems to predate the late-phase of ETE. This apparent diachrony may have resulted from local volcanic activity at QXL, evidence for which is an ~10-cm-thick bentonite bed at ~120 m (Fig. 2). Although the upper ETE interval at QXL does not correlate to the highest Hg/TOC values, this interval is still associated with the relatively high Hg/TOC values of ~500 parts per million (ppm)/% (Fig. 2). Overall, elevated traces of volcanism are recognized in these two terrestrial basins around the ETE interval, linking the extinction to the period of dominant CAMP volcanism.

Multiple lines of evidence for increased S input in the terrestrial basins

Sulfur in terrestrial catchments is mainly derived from weathering bedrock and atmospheric deposition (*60*, *61*). Atmospheric-S deposition is strongly controlled by regional weather patterns and transport pathways with S supplied from seawater spray [δ^{34}S of ~16 to 30‰ for late Triassic seawater; (*44*)], volcanism (~0 to 5‰), or reduced organic compounds [variable but negative relative to seawater; (*60*, *61*)]. Deposition of S from sea spray is controlled by distance to the coast and the prevailing wind directions (*61*). Neither catchment has any evidence of high-S lithologies being present (e.g., black shale and evaporite) (*22*, *48*). The low S content and S/TOC in both sections prior to any increase in Hg (fig. S2) is consistent with a low weathering input of S, enabling the detection of an enhanced atmospheric signal. In addition to source mixing, S isotopes in terrestrial sediments can be substantially kinetically fractionated by the processes of microbial sulfate reduction (MSR), which produces hydrogen sulfide enriched in ^{32}S, creating more negative δ^{34}S values in sediments when these reduced products are fixed as iron sulfides or become bound in organic matter. When sulfate concentrations are low, the MSR isotopic fractionation can be negligible because of near-complete conversion to sulfide, and in this case, the original S-isotopic character of the mixed end-members (bedrock and atmosphere) is retained (*46*). With increasing S input and sulfate concentration, the fractionation can increase, producing a negative isotope excursion in the reduced S preserved in the sediment (*60*). Ultimately, the net effect on the S isotopic composition preserved in the sediment will reflect a combination of source-δ^{34}S, plus any additional fractionation imposed by increases in sulfate concentration and MSR fractionation (*46*, *60*).

DBTs and BNTs are aromatic sulfur compounds found in a variety of crude oils, coals, and sediments (*56*, *62*). Laboratory experiments have demonstrated that carbon catalyzes the reaction between sulfur (in different forms, such as elemental sulfur, H_2S, FeS_2, and H_2SO_4) and biphenyl to form aromatic sulfur compounds (*57*, *58*). The production of these compounds positively correlates with reactants, with excess sulfur required for anomalies of aromatic sulfur compounds because there is insufficient sulfur present in normal biomass (*56*). DBTs and BNTs are resistant to biodegradation and diagenesis (*56*) but thermal maturity can alter their abundance (*35*, *56*). The HJG section has a Tmax (temperature of maximum hydrocarbon yield during Rock-Eval pyrolysis) of ~435°C (*48*), and the Lower Triassic to Middle Jurassic has an R_o (vitrinite reflectance) of 0.5 to 0.7 in the Junggar Basin (*28*, *48*), suggesting low to moderate maturity. Measurements of R_o and the calculated R_o (termed R_c) according to methylphenanthrene index have a range of 0.5 to 1.1 for the Upper Triassic to Lower Jurassic in the Sichuan Basin (*35*). Whereas these data indicate moderate to high maturity, the concentrations of DBTs and BNTs in the QLX section from Sichuan are much higher than those at HJG, suggesting minimal influence of thermal maturity on the latter records as well. Because there is little evidence that thermal processes have affected DBT and BNT concentrations, we view increases in the abundance of these compounds as evidence of increased sulfur abundance at the time of deposition.

Outside of the interval of Hg enrichment at QLX and HJG, baselines of δ^{34}S are stable, and DBTs, BNTs, and S/TOC have low and stable concentrations (Fig. 2 and fig. S2). Although the baselines shift positively by ~3‰ from pre- to post-ETE in both sections (Fig. 2 and figs. S2 and S3), the sulfur isotope baseline values are well within the range for global average weathered sulfate (*63*). These observations indicate stable terrestrial S inputs from bedrock weathering and atmospheric deposition pre– and post–CAMP activity.

The more variable δ^{34}S and peaks of DBTs, BNTs, and S/TOC at HJG and QXL during the interval of elevated Hg/TOC, often with closely coincident peaks in two or more of these parameters, are likely to indicate the delivery of sulfur and other volcanically derived acids and metals from the CAMP activity (Fig. 2). The ETE is associated with some of the largest spikes in DBTs and BNTs, and in the upper ETE interval of both basins, there are marked coupled positive and negative S-isotope excursions (Fig. 2 and fig. S2), although the magnitude of these changes is smaller at HJG. The transient negative change can be explained by some combination of a peak in volcanic S deposition (as evidenced by increased DBTs and BNTs) and increased fractionation as outlined above. With regard to the positive δ^{34}S shifts (Fig. 2 and fig. S2), it is unlikely that they correspond to changes in weathering because a transient change producing a positive sulfur isotope shift is hard to explain for two basins simultaneously and because published Chemical Index of Alteration (CIA) data do not show a consistent relationship with the peak (*51*). Hence, a change in atmospheric S deposition is most likely to explain to the S-isotope negative excursions at the upper ETE interval. Contribution from seawater spray with its even more positive S-isotope signature is an unlikely cause of this change. More possible is a change in the isotope composition of volcanically emitted sulfur driven by the incorporation of sulfur from evaporite gypsum, which has a markedly positive

S-isotope signature. Heimdal *et al.* (*10*) present evidence from Cl concentrations in biotites from CAMP intrusives to suggest widescale incorporation of evaporitic halite, which is likely to have increased overall sulfur emission and deposition. However, our records indicate that this positive excursion occurred in a short interval coincident with the ETE, whereas any thermogenically derived signal would likely persist over an interval coincident with the much longer eruption of CAMP volcanism. Although this feature of the record remains enigmatic, the bulk of the evidence points to a prolonged period of enhanced sulfur deposition during the eruption of CAMP, with a peak in deposition during the ETE.

Increased concentrations of higher plant biomarkers coincident with plant loss

During the Cretaceous-Paleogene boundary crisis, an abrupt increase in the flux of terrestrial organic matter into the ocean was witnessed by an increase of higher plant biomarkers such as retene, pimanthrene, and cadalene (*62*, *64*), suggesting destruction of land vegetation (*62*, *64*). A similar increase of these biomarkers is also seen at HJG during the ETE (*17*). The new dataset from QLX show similar biomarker occurrences to those at HJG and other sites (Fig. 3). Specifically, the abundance of pimanthrene and retene show the highest values at HJG and QLX in the stratigraphic ETE interval. However, these could be due to increased plant biomass or a short-term, catastrophic decline of existing biomass. According to the palynological data from HJG (*23*, *28*) and records of macro-plant fossils and palynological observation at QXL (*22*), the two basins both suffered plant biodiversity loss at the ETE interval and coeval fern spikes (Fig. 2 and fig. S2). Combining all lines of evidence, the high stratigraphic abundance of floral biomarkers demonstrates a critical destruction of terrestrial biomass at HJG and QXL profiles. Other terrestrial and shallow marine sections show a similar story derived from palynological records (Fig. 3) (*12*). This extensive terrestrial biological catastrophe lasted ~60 kyr and coincided with the CAMP climax indicated by the highest peaks of Hg/TOC.

Intense wildfires during the ETE

Fluoranthene-to-pyrene ratios [Fl/(Fl + Py)] are commonly used to distinguish between different sources of PAHs (*65*, *66*). In the HJG and QLX sections, Fl/(Fl + Py) values are predominantly distributed within the 0.4-to-0.5 and >0.5 ranges, whereas values <0.4 account for a minor proportion (fig. S5), suggesting that PAHs in both sections were mainly derived from pyrogenic sources. Coronene is a highly condensed, six-ring PAH that requires greater energy to form than lower–molecular weight PAHs (*36*). In geological and environmental contexts, elevated coronene abundances or high coronene indexes [>0.3; defined as coronene/(benzo[*e*]pyrene + benzo[*ghi*]perylene + coronene)] are indicative of high-temperature processes (>1000°C), typically associated with intense combustion or volcanic activity (*21*, *36*). Although coronene and other PAHs may be degraded by soil microorganisms (mainly fungi) under oxidizing conditions prior to burial, they are generally resistant in the geological record (*21*, *36*, *67*). The woody part of living trees burns at ~400° to 700°C but rarely >1000°C under natural conditions, because temperature rise is limited by an equilibrium between moisture content and efficiency of heat release [e.g., (*68*)]. However, combustion records of >1000° to 1200°C are recorded by a coronene index of 0.3 to 0.4 at the Tr-J GSSP Kuhjoch section, Austria, coinciding with the Hg/TOC peaks (i.e., CAMP climax) (*36*). The highest peaks of coronene and coronene/Bap ratios demonstrate that enhanced wildfires occurred at HJG and QLX at the same time (Fig. 3). The maximum peaks of DBTs and BNTs, with peaks of Hg/TOC ratio, coincide with the intense eruptions of the CAMP climax (Figs. 2 and 3). Collectively, widespread and intensified wildfires appear to coincide temporally with acid rain, rapid influxes of terrestrial biomass, biodiversity loss (*17*), and the most intense phases of CAMP volcanic activity, all of which occurred within a narrow interval (~60 kyr) in terrestrial ecosystems (Fig. 3). These phenomena likely operated on a regional to global scale, driven by long-range atmospheric transport of volcanic volatile emissions.

Mechanism of terrestrial crisis during the end-Triassic

The release of volcanism-derived S (plus HCl, HF, etc.), leading to acid rain, may have played a vital role in the end-Triassic terrestrial crisis. The CAMP volcanism lasted for ~600 kyr and consisted of four major eruptive pulses (*2*, *6*), with total emissions of SO_2 up to 16,000 to 32,000 gigatonnes (*7*), but the most intense eruption took place within ~60 kyr (*6*). The subsequent formation of sulfate aerosols led to acid rain precipitation, which stressed the terrestrial flora and caused widespread vegetation collapse. The acid rain/mists could directly harm plant growth (*69*–*71*) and alter soils to affect root health (*72*). This mechanism is analogous to the quantitative modeling of Deccan Trap sulfur emissions, which shows that, at peak intensity, these emissions lethally harm up to 44% of the land surface (*40*). When the maximum intensity of CAMP volcanism took place, the soil buffering capacity in the HJG and QLX hinterland might have declined to lethal levels, owing to repeated pluses of acid rain precipitation in a relatively short time. Even if soil pH only declines from 7 to 5, the phosphorus nutrition necessary for plant growth (*73*) and vital metal cation (e.g., Ca^{2+}, Mg^{2+}, K^{+}, and Na^{+}) (*74*) becomes more soluble and prone to transport, within a few weeks (*73*) and days (*74*), respectively. This, together with the possibility of intervals of intense drought associated with climate change (*18*) and strong seasonality (*75*), is likely to have increased the frequency and intensity of wildfires. Contemporaneous with the intense acid rain, the effusion of heavy metals during volcanism may also have poisoned plants (*11*), and volcanic winters associated with S release have also been mooted as a stress on terrestrial ecosystems (*1*). These combined factors likely led terrestrial primary productivity to collapse, creating massive fuel stores for intense wildfires over large areas (Figs. 2 and 3), with these cycles of regrowth, mortality, and wildfire happening repeatedly in multiple cycles. The widely preexisting forest mortality can drive subsequent wildfires and/or soil erosion, as observed in modern cases (*76*). The pervasive and abnormally intense high-temperature wildfires during the ETE interval were more likely a consequence of terrestrial ecosystem collapse [e.g., modern analogs of biomass destruction followed by severe wildfires; (*76*)], rather than a primary driver of the crisis, as suggested in previous work (*77*).

Because SO_2 has a short atmospheric residence time, it is rapidly removed and delivered directly to land-surface reservoirs, which generally have far lower sulfur-buffering capacity than in the oceans. Our ETE case study provides geological evidence consistent with this atmospheric-chemistry principle by showing that terrestrial ecosystems become highly vulnerable when sulfur loading increases faster than soils and vegetation can buffer chemical changes. Recognizing this linkage offers a useful framework for understanding how terrestrial and marine systems may respond differently to rapid sulfur-driven

atmospheric perturbations arising from volcanic activity or anthropogenic emissions today.

MATERIALS AND METHODS

Materials

We collected samples from two terrestrial Tr-J sections in northwest (HJG section in Xinjiang Province) and south (QLX section in Sichuan Province) China (fig. S1). No permits were required for the collection of geological samples used in this study. The sampling stratigraphic positions, lithological description, and all their results are presented in Figs. 2 and 3, the Supplementary Materials, and data tables. Weathered surfaces and veins were removed from the samples, which were then ultrasonicated in distilled water three times and dried at 55°Cfor 24 hours.

Bulk sulfur extraction and isotope analysis

Total sulfur, including metal-bound S (primarily FeS_2) and organosulfur compounds, was extracted using the Eschka fusion technique. About 6 g of sample was mixed with 6 g of Eschka's mixture ($MgO:Na_2CO_3 = 2:1$), covered with an additional ~1 g of Eschka's mixture, and heated in corundum crucibles, at 3°C/min to 850°C for 2 hours. The fused material was extracted with ~80°C deionized water and filtered, and the filtrate was acidified with 6 to 7 ml of 36% HCl and then boiled, cooled, and treated with 25 ml of $BaCl_2$ to precipitate $BaSO_4$. After settling overnight, $BaSO_4$ was filtered, rinsed, dried, and weighed. Blanks were run alongside samples. The $^{34}S/^{32}S$ ratio of sulfur extractions ($BaSO_4$ precipitate) was measured using an Elementar Pyrocube coupled to an isoprime continuous flow mass spectrometer, following published procedures (*46*). All samples were analyzed in duplicate, with reproducibility better than ±0.3‰ (1 SD). All sulfur extractions and isotope analysis were performed in the Cohen Laboratories, School of Earth and Environment, University of Leeds.

Biomarker extraction and analysis

Samples from the HJG section were extracted by Soxhlet. Approximately 100 g of powdered subsamples (~200 mesh) were extracted for 24 hours using 300 ml of dichloromethane. Samples from the QLX section were extracted using accelerated solvent extraction (ASE 350). Approximately 20 g of powdered subsamples (~200 mesh) were extracted in ASE cells with dichloromethane at 100°C, with a heating time of 5 min and a static time of 5 min. The rinse volume was set to 50%, the purge time was 70 s, and the static cycle was repeated three times. All extracts were concentrated by rotary evaporation, and asphaltenes were precipitated using petroleum ether. The remaining solutions were separated into saturated and aromatic hydrocarbon fractions by column chromatography, using a silica gel:alumina (3:2, v/v) column. The fractions were eluted with 30 ml of petroleum ether and 20 ml of dichloromethane:petroleum ether (2:1, v/v), respectively. Saturated and aromatic hydrocarbons were analyzed using Agilent 7890/5975i and Agilent 7890B/5977 gas chromatography–mass spectrometry (GC-MS) systems equipped with HP-5MS fused-silica columns. Temperature programs, internal standards (D50C24 and D10P), GC-MS operating conditions, and chromatography procedures follow the protocols described in published literature (*17*). All measurements were conducted at the State Key Laboratory of Petroleum Resources and Engineering, China University of Petroleum (Beijing).

TOC (wt %) and total sulfur (wt %)

Powdered subsample (~200 mesh) was treated with 10% HCl at 55°C for 12 hours to remove carbonates, rinsed to neutral pH, dried at 55°C, and mixed with 1 g each of iron and tungsten fluxes. TOC and total sulfur (TS) were measured using a LECO CS230 Carbon-Sulphur Analyzer. Analytical precision is better than 100 ppm for TOC and 10 ppm for TS. Data quality was monitored via replicate analyses of laboratory working standards, with reproducibility (2σ) of ±3% for carbon and ±10% for sulfur; standards were run at the beginning and end of each 15-sample batch. All experiments were conducted at the State Key Laboratory of Petroleum Resources and Engineering, China University of Petroleum (Beijing).

Mercury concentration

A 0.25-g subsample (~200 mesh) was weighed into 25 ml of polyethylene tube, wetted with deionized water, and digested with 10 ml (1 + 1) of aqua regia in a 100°C water bath for 1 hour, with shaking once at 30 min. After cooling, 1 ml of $KMnO_4$ solution (10 g/liter) was added for 30 min, and then, the solution was diluted with oxalic acid (10 g/liter) to 25 ml. A 2-ml aliquot was used for Hg analysis. Mercury concentrations were measured by cold vapor atomic fluorescence spectrometry (AFS-8510) using a quartz atomizer preheated to 200°C and argon carrier gas (99.9999%), with a detection limit of 0.3 parts per billion (ppb) and a working range of 1 to 6000 ppb. One replicate and one standard were analyzed per 10 samples, and results were calibrated against three standards of soil composition reference material GBW07449(GSS-20) (8 ± 2 ppb Hg), GBW07453(GSS-24) (75 ± 7 ppb Hg), and GBW07385(GSS-29) (150 ± 20 ppb Hg). Measurements were conducted at the Hebei Institute of Geophysical and Geochemical Exploration, Chinese Academy of Geological Sciences.

Supplementary Materials

The PDF file includes:

Supplementary Text
Figs. S1 to S6
Legends for tables S1 and S2
Legends for data files S1 and S2
References

Other Supplementary Material for this manuscript includes the following:

Tables S1 and S2
Data files S1 and S2

REFERENCES

1. B. Schoene, J. Guex, A. Bartolini, U. Schaltegger, T. J. Blackburn, Correlating the end-Triassic mass extinction and flood basalt volcanism at the 100 ka level. *Geology* **38**, 387–390 (2010).
2. T. J. Blackburn, P. E. Olsen, S. A. Bowring, N. M. McLean, D. V. Kent, J. Puffer, G. McHone, E. T. Rasbury, M. Et-Touhami, Zircon U-Pb geochronology links the end-Triassic extinction with the Central Atlantic Magmatic Province. *Science* **340**, 941–945 (2013).
3. J. J. Sepkoski, A factor analytic description of the Phanerozoic marine fossil record. *Paleobiology* **7**, 36–53 (1981).
4. P. B. Wignall, J. W. Atkinson, A two-phase end-Triassic mass extinction. *Earth Sci. Rev.* **208**, 103282 (2020).
5. A. Marzoli, S. Callegaro, J. Dal Corso, J. H. Davies, M. Chiaradia, N. Youbi, H. Bertrand, L. Reisberg, R. Merle, F. Jourdan, "The Central Atlantic Magmatic Province (CAMP): A review" in *The Late Triassic World: Earth in a Time of Transition*, L. Tanner, Ed. (Springer, 2018), pp. 91–125.
6. A. M. Thibodeau, K. Ritterbush, J. A. Yager, A. J. West, Y. Ibarra, D. J. Bottjer, W. M. Berelson, B. A. Bergquist, F. A. Corsetti, Mercury anomalies and the timing of biotic recovery following the end-Triassic mass extinction. *Nat. Commun.* **7**, 11147 (2016).
7. S. Callegaro, D. R. Baker, A. De Min, A. Marzoli, K. Geraki, H. Bertrand, C. Viti, F. Nestola, Microanalyses link sulfur from large igneous provinces and Mesozoic mass extinctions. *Geology* **42**, 895–898 (2014).

8. M. Capriolo, A. Marzoli, L. E. Aradi, S. Callegaro, J. Dal Corso, R. J. Newton, B. J. Mills, P. B. Wignall, O. Bartoli, D. R. Baker, N. Youbi, Deep CO_2 in the end-Triassic Central Atlantic Magmatic Province. *Nat. Commun.* **11**, 1670 (2020).
9. J. G. McHone, Volatile emissions from Central Atlantic Magmatic Province basalts: Mass assumptions and environmental consequences. *Geophys. Monogr. Am. Geophys. Union* **136**, 241–254 (2003).
10. T. H. Heimdal, S. Callegaro, H. H. Svensen, M. T. Jones, E. Pereira, S. Planke, Evidence for magma-evaporite interactions during the emplacement of the Central Atlantic Magmatic Province (CAMP) in Brazil. *Earth Planet. Sci. Lett.* **506**, 476–492 (2019).
11. S. Lindström, H. Sanei, B. V. D. Schootbrugge, G. K. Pedersen, P. M. Outridge, Volcanic mercury and mutagenesis in land plants during the end-Triassic mass extinction. *Sci. Adv.* **2**, eaaw4018 (2019).
12. S. Lindström, Two-phased mass rarity and extinction in land plants during the end-Triassic climate crisis. *Front. Earth Sci.* **9**, 780343 (2021).
13. J. C. McElwain, P. Wagner, S. P. Hesselbo, Fossil plant relative abundances indicate sudden loss of Late Triassic biodiversity in East Greenland. *Science* **324**, 1554–1556 (2009).
14. W. K. Soh, I. J. Wright, K. L. Bacon, T. I. Lenz, M. Steinthorsdottir, A. C. Parnell, J. C. McElwain, Palaeo leaf economics reveal a shift in ecosystem function associated with the end-Triassic mass extinction event. *Nat. Plants* **3**, 1–8 (2017).
15. S. J. Fowell, B. Cornet, P. E. Olsen, Geologically rapid Late Triassic extinctions: Palynological evidence from the Newark Supergroup. Pangaea: Paleoclimate, tectonics and sedimentation during accretion, zenith and break-up of a supercontinent. *Geol. Soc. Am. Sp.* **288**, 197–206 (1994).
16. N. R. Bonis, M. Ruhl, W. M. Kürschner, Milankovitch-scale palynological turnover across the Triassic-Jurassic transition at St. Audrie's Bay, SW UK. *J. Geol. Soc. London* **167**, 877–888 (2010).
17. X. Zhang, P. Lv, L. Fang, G. Wang, Y. Lu, S. Deng, H. Yang, Y. Fang, H. Li, X. Zhang, Y. Sun, Biomarker evidence for deforestation across the Triassic-Jurassic boundary in the high palaeolatitude Junggar Basin, northwest China. *Palaeogeogr. Palaeoclimatol. Palaeoecol.* **600**, 111074 (2022).
18. N. R. Bonis, W. M. Kürschner, Vegetation history, diversity patterns, and climate change across the Triassic/Jurassic boundary. *Paleobiology* **38**, 240–264 (2012).
19. X. Z. Zhang, L. H. Fang, T. Wu, Y. F. Miao, M. Z. Zhang, X. L. Wang, P. Z. Lv, X. J. He, R. Y. Qiu, H. Yang, J. H. Ren, Palynological assemblages and palaeoclimate across the Triassic-Jurassic boundary in the Haojiagou section, southern Junggar Basin. *Chin. J. Geol.* **57**, 1–16 (2022).
20. H. I. Petersen, S. Lindström, Synchronous wildfire activity rise and mire deforestation at the Triassic-Jurassic boundary. *PLOS ONE* **7**, e47236 (2012).
21. B. Van de Schootbrugge, M. Quan, S. Lindström, W. Püttmann, C. Heunisch, J. Pross, J. Fiebig, R. Petschick, H. G. Röhling, S. Richoz, Y. Rosenthal, P. G. Falkowski, Floral changes across the Triassic/Jurassic boundary linked to flood basalt volcanism. *Nat. Geosci.* **2**, 589–594 (2009).
22. L. Li, Y. Wang, W. M. Kürschner, M. Ruhl, V. Vajda, Palaeovegetation and palaeoclimate changes across the Triassic-Jurassic transition in the Sichuan Basin, China. *Palaeogeogr. Palaeoclimatol. Palaeoecol.* **556**, 109891 (2020).
23. Y. Lu, S. Deng, Palaeoclimate around the Triassic-Jurassic Boundary in southern margin of Junggar Basin. *J. Palaeogeog.* **11**, 652–660 (2009).
24. J. P. Landwehrs, G. Feulner, M. Hofmann, S. Petri, Climatic fluctuations modeled for carbon and sulfur emissions from end-Triassic volcanism. *Earth Planet. Sci. Lett.* **537**, 116174 (2020).
25. E. Buffetaut, "Continental vertebrate extinctions at the Triassic-Jurassic and Cretaceous-Tertiary boundaries: A comparison" in *Biological Processes Associated with Impact Events* (Springer, 2006), pp. 245–256.
26. M. Steinthorsdottir, A. M. P. Tosolini, J. C. Mcelwain, Evidence for insect and annelid activity across the Triassic-Jurassic transition of east Greenland. *Palaios* **30**, 597–607 (2015).
27. T. J. B. van Eldijk, T. Wappler, P. K. Strother, C. M. H. van der Weijst, H. Rajaei, H. Visscher, B. van de Schootbrugge, A Triassic-Jurassic window into the evolution of *Lepidoptera*. *Sci. Adv.* **4**, e1701568 (2018).
28. X. Z. Zhang, P. Z. Lv, L. H. Fang, H. Yang, S. H. Deng, Y. Z. Lu, Y. N. Fang, X. Y. Zhang, R. T. Huang, J. B. Liang, S. B. Shi, Wildfire records across the Triassic-Jurassic boundary in the southern margin of the Junggar Basin and global correlations. *Acta Sedimentol. Sin.* **40**, 473–483 (2022).
29. J. C. McElwain, D. J. Beerling, F. I. Woodward, Fossil plants and global warming at the Triassic-Jurassic boundary. *Science* **285**, 1386–1390 (1999).
30. M. Steinthorsdottir, A. J. Jeram, J. C. McElwain, Extremely elevated CO_2 concentrations at the Triassic/Jurassic boundary. *Palaeogeogr. Palaeoclimatol. Palaeoecol.* **308**, 418–432 (2011).
31. C. M. Belcher, L. Mander, G. Rein, F. X. Jervis, M. Haworth, S. P. Hesselbo, L. J. Glasspool, J. C. McElwain, Increased fire activity at the Triassic/Jurassic boundary in Greenland due to climate-driven floral change. *Nat. Geosci.* **3**, 426–429 (2010).
32. M. F. Schaller, J. D. Wright, D. V. Kent, Atmospheric pCO_2 perturbations associated with the Central Atlantic Magmatic Province. *Science* **331**, 1404–1409 (2011).
33. S. P. Hesselbo, S. A. Robinson, F. Surlyk, S. Piasecki, Terrestrial and marine extinction at the Triassic-Jurassic boundary synchronized with major carbon-cycle perturbation: A link to initiation of massive volcanism? *Geology* **30**, 251–254 (2002).
34. K. H. Williford, K. Grice, A. Holman, J. C. McElwain, An organic record of terrestrial ecosystem collapse and recovery at the Triassic-Jurassic boundary in East Greenland. *Geochim. Cosmochim. Acta* **127**, 251–263 (2014).
35. Y. Song, T. J. Algeo, W. Wu, G. Luo, S. Xie, Distribution of pyrolytic PAHs across the Triassic-Jurassic boundary in the Sichuan Basin, southwestern China: Evidence of wildfire outside the Central Atlantic Magmatic Province. *Earth Sci. Rev.* **201**, 102970 (2020).
36. K. Kaiho, D. Tanaka, S. Richoz, D. S. Jones, R. Saito, D. Kameyama, M. Ikeda, S. Takahashi, M. Aftabuzzaman, M. Fujibayashi, Volcanic temperature changes modulated volatile release and climate fluctuations at the end-Triassic mass extinction. *Earth Planet. Sci. Lett.* **579**, 117364 (2022).
37. S. Lindström, S. Callegaro, J. Davies, C. Tegner, B. van De Schootbrugge, G. K. Pedersen, N. Youbi, H. Sanei, A. Marzoli, Tracing volcanic emissions from the Central Atlantic Magmatic Province in the sedimentary record. *Earth Sci. Rev.* **212**, 103444 (2021).
38. B. Van de Schootbrugge, C. M. H. Van Der Weijst, T. P. Hollaar, M. Vecoli, P. K. Strother, N. Kuhlmann, J. Thein, H. Visscher, H. van Konijnenburg-van Cittert, M. A. N. Schobben, A. Sluijs, S. Lindström, Catastrophic soil loss associated with end-Triassic deforestation. *Earth Sci. Rev.* **210**, 103332 (2020).
39. S. Self, M. Widdowson, T. Thordarson, A. E. Jay, Volatile fluxes during flood basalt eruptions and potential effects on the global environment: A Deccan perspective. *Earth Planet. Sci. Lett.* **248**, 518–532 (2006).
40. A. Schmidt, R. A. Skeffington, T. Thordarson, S. Self, P. M. Forster, A. Rap, A. Ridgwell, D. Fowler, M. Wilson, G. W. Mann, P. B. Wignall, Selective environmental stress from sulphur emitted by continental flood basalt eruptions. *Nat. Geosci.* **9**, 77–82 (2016).
41. A. Robock, C. Oppenheimer, *Volcanism and the Earth's Atmosphere* (American Geophysical Union, 2003), vol. 139.
42. M. J. Mills, A. Schmidt, R. Easter, S. Solomon, D. E. Kinnison, S. J. Ghan, R. R. Neely III, D. R. Marsh, A. Conley, C. G. Bardeen, A. Gettelman, Global volcanic aerosol properties derived from emissions, 1990–2014, using CESM1 (WACCM). *J. Geophys. Res. Atmos.* **121**, 2332–2348 (2016).
43. R. P. Singh, M. Agrawal, Variations in heavy metal accumulation, growth and yield of rice plants grown at different sewage sludge amendment rates. *Ecotox. Environ. Safe.* **73**, 632–641 (2010).
44. T. He, J. D. Corso, R. J. Newton, P. B. Wignall, A. M. Dunhill, An enormous sulfur isotope excursion indicates marine anoxia during the end-Triassic mass extinction. *Sci. Adv.* **6**, eabb6704 (2020).
45. R. Newton, S. Bottrell, Stable isotopes of carbon and sulphur as indicators of environmental change: Past and present. *J. Geol. Soc. London* **164**, 691–708 (2007).
46. J. Dal Corso, R. J. Newton, A. L. Zerkle, D. Chu, H. Song, H. Song, L. Tian, J. Tong, T. Di Rocco, M. W. Claire, T. A. Mather, T. He, T. Gallagher, W. Shu, Y. Wu, S. H. Bottrell, I. Metcalfe, H. A. Cope, M. Novak, R. A. Jamieson, P. B. Wignall, Repeated pulses of volcanism drove the end-Permian terrestrial crisis in northwest China. *Nat. Commun.* **15**, 7628 (2024).
47. M. Steinthorsdottir, C. Elliott-Kingston, K. L. Bacon, Cuticle surfaces of fossil plants as a potential proxy for volcanic SO_2 emissions: Observations from the Triassic-Jurassic transition of East Greenland. *Palaeobio. Palaeoenv.* **98**, 49–69 (2018).
48. Y. Fang, L. Fang, S. Deng, Y. Lu, B. Wang, X. Zhao, Y. Wang, H. Zhang, X. Zhang, J. Sha, Carbon isotope stratigraphy across the Triassic-Jurassic boundary in the high-latitude terrestrial Junggar Basin, NW China. *Palaeogeogr. Palaeoclimatol. Palaeoecol.* **577**, 110559 (2021).
49. S. Deng, Y. Lu, R. Fan, Y. Pan, X. Cheng, G. Fu, Q. Wang, H. Pan, Y. Shen, Y. Wang, W. Duan, H. Zhang, C. Jia, L. Fang, *The Jurassic System of Northern Xinjiang, China* (Science and Technology Univ. Press, 2010).
50. J. Sha, P. E. Olsen, Y. Pan, D. Xu, Y. Wang, X. Zhang, X. Yao, Triassic-Jurassic climate in continental high-latitude Asia was dominated by obliquity-paced variations (Junggar Basin, Urumqi, China). *Proc. Natl. Acad. Sci. U.S.A.* **112**, 3624–3629 (2015).
51. J. Shen, R. Yin, S. Zhang, T. J. Algeo, D. J. Bottjer, J. Yu, G. Xu, D. Penman, Y. Wang, L. Li, X. Shi, Intensified continental chemical weathering and carbon-cycle perturbations linked to volcanism during the Triassic-Jurassic transition. *Nat. Commun.* **13**, 299 (2022).
52. M. Li, Y. Zhang, C. Huang, J. Ogg, L. Hinnov, Y. Wang, Z. Zou, L. Li, Astronomical tuning and magnetostratigraphy of the Upper Triassic Xujiahe Formation of South China and Newark Supergroup of North America: Implications for the Late Triassic time scale. *Earth Planet. Sci. Lett.* **475**, 207–223 (2017).
53. J. Shen, Q. Feng, T. J. Algeo, J. Liu, C. Zhou, W. Wei, J. Liu, T. R. Them II, B. C. Gill, J. Chen, Sedimentary host phases of mercury (Hg) and implications for use of Hg as a volcanic proxy. *Earth Planet. Sci. Lett.* **543**, 116333 (2020).
54. J. A. Yager, A. J. West, A. M. Thibodeau, F. A. Corsetti, M. Rigo, W. M. Berelson, D. J. Bottjer, S. E. Greene, Y. Ibarra, F. Jadoul, K. A. Ritterbush, Mercury contents and isotope ratios from diverse depositional environments across the Triassic-Jurassic Boundary: Towards a more robust mercury proxy for large igneous province magmatism. *Earth Sci. Rev.* **223**, 103775 (2021).

55. L. M. Percival, M. Ruhl, S. P. Hesselbo, H. C. Jenkyns, T. A. Mather, J. H. Whiteside, Mercury evidence for pulsed volcanism during the end-Triassic mass extinction. *Proc. Natl. Acad. Sci. U.S.A.* **114**, 7929–7934 (2017).
56. D. Oliveira, L. M. Leoncio, D. N. Amaral, K. L. A. Ferreira, C. S. Souza, G. M. Hadlich, M. E. Machado, Polycyclic aromatic sulfur heterocycles used as molecular markers in crude oils and source rocks. *Org. Geochem.* **178**, 104571 (2023).
57. V. K. Olkhovik, D. A. Vasilevskii, A. A. Pap, G. V. Kalechyts, Y. V. Matveienko, A. G. Baran, N. A. Halinouski, V. G. Petushok, Synthesis of new polyconjugated molecules with biphenyl, dibenzothiophene, carbazole and phenanthrene units. *ARKIVOC* **2008**, 69–93 (2009).
58. M. Asif, R. Alexander, T. Fazeelat, K. Pierce, Geosynthesis of dibenzothiophene and alkyl dibenzothiophenes in crude oils and sediments by carbon catalysis. *Org. Geochem.* **40**, 895–901 (2009).
59. K. Kaiho, M. Aftabuzzaman, D. S. Jones, L. Tian, Pulsed volcanic combustion events coincident with the end-Permian terrestrial disturbance and the following global crisis. *Geology* **49**, 289–293 (2021).
60. M. Li, T. D. Frank, Y. Xu, C. R. Fielding, Y. Gong, Y. Shen, Sulfur isotopes link atmospheric sulfate aerosols from the Siberian Traps outgassing to the end-Permian extinction on land. *Earth Planet. Sci. Lett.* **592**, 117634 (2022).
61. L. Newman, H. R. Krouse, V. A. Grinenko, "Sulphur isotope variations in the atmosphere" in *Stable Isotopes: Natural and Anthropogenic Sulphur in the Environment*, H. R. Krouse, V. A. Grinenko, Eds. (John Wiley and Sons, 1991), vol. SCOPE 43, pp. 133–176).
62. T. Mizukami, K. Kaiho, M. Oba, Significant changes in land vegetation and oceanic redox across the Cretaceous/Paleogene boundary. *Palaeogeogr. Palaeoclimatol. Palaeoecol.* **369**, 41–47 (2013).
63. A. Burke, T. M. Present, G. Paris, E. C. Rae, B. H. Sandilands, J. Gaillardet, B. Peucker-Ehrenbrink, W. W. Fischer, J. W. McClelland, R. G. Spencer, B. M. Voss, Sulfur isotopes in rivers: Insights into global weathering budgets, pyrite oxidation, and the modern sulfur cycle. *Earth Planet. Sci. Lett.* **496**, 168–177 (2018).
64. T. Mizukami, K. Kaiho, M. Oba, A spike of woody plant biomarkers in the deep-sea iridium layer at the Cretaceous/Paleogene boundary. *Palaeogeogr. Palaeoclimatol. Palaeoecol.* **412**, 241–248 (2014).
65. C. P. Fox, J. H. Whiteside, P. E. Olsen, K. Grice, Flame out! End-Triassic mass extinction polycyclic aromatic hydrocarbons reflect more than just fire. *Earth Planet. Sci. Lett.* **584**, 117418 (2022).
66. M. B. Yunker, R. W. Macdonald, R. Vingarzan, R. H. Mitchell, D. Goyette, S. Sylvestre, PAHs in the Fraser River basin: A critical appraisal of PAH ratios as indicators of PAH source and composition. *Org. Geochem.* **33**, 489–515 (2002).
67. X. X. Zhang, S. P. Cheng, C. J. Zhu, S. L. Sun, Microbial PAH-degradation in soil: Degradation pathways and contributing factors. *Pedosphere* **16**, 555–565 (2006).
68. C. D. Blasi, Modeling and simulation of combustion processes of charring and non-charring solid fuels. *Prog. Energ. Combust.* **19**, 71–104 (1993).
69. W. E. Winner, H. A. Mooney, Responses of Hawaiian plants to volcanic sulfur dioxide: Stomatal behavior and foliar injury. *Science* **210**, 789–791 (1980).
70. P. Delmelle, T. Delfosse, B. Delvaux, Sulfate, chloride and fluoride retention in Andosols exposed to volcanic acid emissions. *Environ. Pollut.* **126**, 445–457 (2003).
71. K. L. Bacon, C. M. Belcher, M. Haworth, J. C. McElwain, Increased atmospheric SO_2 detected from changes in leaf physiognomy across the Triassic-Jurassic boundary interval of East Greenland. *PLOS ONE* **8**, e60614 (2013).
72. P. Delmelle, J. Stix, C. P. A. Bourque, P. J. Baxter, J. G. Alvarez, J. Barquero, Dry deposition and heavy acid loading in the Vicinity of Masaya Volcano, a major sulfur and chlorine source in Nicaragua. *Environ. Sci. Technol.* **35**, 1289–1293 (2001).
73. M. Islam, K. H. Siddique, L. P. Padhye, J. Pang, Z. M. Solaiman, D. Hou, C. Srinivasarao, T. Zhang, P. Chandana, N. Venu, J. V. N. S. Prasad, A critical review of soil phosphorus dynamics and biogeochemical processes for unlocking soil phosphorus reserves. *Adv. Agron.* **185**, 153–249 (2024).
74. M. Jalali, E. N. Peikam, Measuring and simulating the effect of acid rain on cations leaching from calcareous soil of Western Iran. *Arab. J. Geosci.* **15**, 1194 (2022).
75. V. A. Petryshyn, S. E. Greene, A. Farnsworth, D. J. Lunt, A. Kelley, R. Gammariello, Y. Ibarra, D. J. Bottjer, A. Tripati, F. A. Corsetti, The role of temperature in the initiation of the end-Triassic mass extinction. *Earth Sci. Rev.* **208**, 103266 (2020).
76. J. T. Abatzoglou, A. P. Williams, Impact of anthropogenic climate change on wildfire across western US forests. *Proc. Natl. Acad. Sci. U.S.A.* **113**, 11770–11775 (2016).
77. P. Zhang, M. Yang, Z. Jiang, K. Zhou, X. Xu, H. Chen, X. Zhu, Y. Guo, H. Ye, Y. Zhang, L. Shao, Significant floral changes across the Permian–Triassic and Triassic-Jurassic transitions induced by widespread wildfires. *Front. Ecol. Evol.* **11**, 1284482 (2023).
78. M. Li, L. Hinnov, L. Kump, Acycle: Time-series analysis software for paleoclimate research and education. *Comput. Geosci.* **127**, 12–22 (2019).

Acknowledgments: We thank M. Li for the assistance with reanalyzing LITH index data cited from previous works to replot a floating astrochronological scale. **Funding:** This study was funded by the National Natural Science Foundation of China (grant nos. 42472154 to L.F., 42372130 to T.H., and 41925010 to H.W.), the 111 Project (B20011 to H.W.), and the Fund of Outstanding Youth, China University of Petroleum (Beijing) (grant no. 2462014YJRC027 to L.F.). **Author contributions:** Conceptualization: L.F., R.J.N., and Y.L. Investigation: L.F., S.S., S.D., H.L., and S.H.B. Methodology: G.W., R.J.N., S.S., S.H.B., M.L., H.W., H.L., L.Z., and L.F. Resources: L.F., R.J.N., and S.H.B. Data curation: G.W., X.Z., C.Z., and L.F. Formal analysis: L.F., G.W., X.Z., C.Z., S.S., H.L., and L.Z. Validation: G.W., S.S., M.L., H.W., L.Z., H.L., and L.F. Software: L.F. Visualization: P.B.W., L.F., X.Z., H.L., and C.Z. Supervision: L.F., R.J.N., and G.W. Project administration: L.F. and R.J.N. Funding acquisition: L.F., T.H., G.W., and H.W. Writing—original draft: L.F., R.J.N., T.H., and P.B.W. Writing—review and editing: S.P.H., P.B.W., B.X., G.W., S.H.B., T.H., H.W., S.D., H.L., R.J.N., and L.F. **Competing interests:** The authors declare that they have no competing interests. **Data, code, and materials availability:** All data and code needed to evaluate and reproduce the results in the paper are present in the paper and/or the Supplementary Materials. The geochemical datasets generated and analyzed in this study are provided in data files S1 and S2. Geological samples were collected by the authors and are stored at China University of Petroleum (Beijing). No formal accession numbers are assigned; samples are cataloged using internal identifiers consistent with those reported in this study.

Submitted 14 June 2025
Accepted 19 March 2026
Published 13 May 2026
10.1126/sciadv.adz6570

ScienceAdvances

Pulsed volcanic sulfur emissions linked to the end-Triassic terrestrial crisis

Linhao Fang, Robert J. Newton, Xiaoyu Zhang, Hongjia Li, Guangli Wang, Shenghui Deng, Paul B. Wignall, Yuanzheng Lu, Chaokun Zhang, Meijun Li, Huaichun Wu, Tianchen He, Benzhong Xian, Shengbao Shi, Lei Zhu, Simon H. Bottrell, and Stephen P. Hesselbo

Sci. Adv. **12** (20), eadz6570. DOI: 10.1126/sciadv.adz6570

Science Advances (ISSN 2375-2548) is published by the American Association for the Advancement of Science. 1200 New York Avenue NW, Washington, DC 20005. The title *Science Advances* is a registered trademark of AAAS.